Acta Geodyn. Geomater., Vol. 22, No. 4 (220), 473–484, 2025
DOI: 10.13168/AGG.2025.0034
journal homepage: https://www.irsm.cas.cz/acta

ORIGINAL PAPER

RAPID INVERSION OF SOURCE FOR THE 2021 CHIGNIK, ALASKA EARTHQUAKE USING HIGH-RATE GNSS OBSERVATIONS

Yunfei XIANG [1, 2] *, Lei HONG [2], Ming QIN [2] and Yankai BIAN [3]

[1] *College of Oceanography, Hohai University, Nanjing 210024, China*
[2] *Department of Geomatics Engineering, Nanjing Forestry University, Nanjing 210037, China*
[3] *School of Geomatics, Zhejiang University of Water Resources and Electric Power, Hangzhou 310018, China*

**Corresponding author's e-mail:* yfxiang@njfu.edu.cn

ARTICLE INFO

Article history:
Received 20 May 2025
Accepted 2 October 2025
Available online 4 November 2025

Keywords:
High-rate GNSS
Coseismic deformation
The first arrival of seismic waves
Moment magnitude
Coseismic slip distribution

ABSTRACT

Based on the records of 1 Hz GNSS sites, the coseismic static and dynamic deformations of the 2021 M 8.2 Chignik, Alaska earthquake is detected, and the source parameters are rapidly inverted using coseismic deformations. Firstly, the Smoothness Priors Method (SPM) is adopted to extract the coseismic static deformations from GNSS displacement time series. The result is highly consistent with the coseismic offsets provided by the EarthScope Consortium, indicating that high-rate GNSS can rapidly determine coseismic static deformations. On the basis of the GNSS velocity time series, the S-transform is utilized to detect the first arrival time of seismic waves at each site in the time-frequency domain. Subsequently, the moment magnitude of this earthquake is determined according to the empirical regression model and GNSS-derived Peak Ground Displacement (PGD), which differs by 0.46 magnitude from the reference magnitude provided by United States Geological Survey (USGS). The convergence time of the average moment magnitude inverted by the nine sites is 117 s, indicating that a robust and reliable magnitude can be obtained by the near-field GNSS sites with about 117 s after the earthquake. Finally, the coseismic rupture distribution of this earthquake is estimated using coseismic deformations and constructed fault model. The coseismic slip distribution is concentrated in the depth range of 20 and 50 km with the maximum value of 3.87 m, which is situated at the longitude of 157.57° W, the latitude of 55.47° N, and the depth of 33.89 km.

1. INTRODUCTION

Among natural disasters, seismic disasters occur more frequently, which have the largest effect on the development of human society. Strong ground movements, tsunamis, and secondary disasters induced by the strong earthquake have brought huge casualties and economic losses to human society. Due to the complex geophysical mechanism of earthquakes, accurate earthquake prediction is still unattainable up to now, and the Earthquake Early Warning (EEW) technology is an effective means to reduce the losses caused by the earthquake (Man et al., 2009; Zhang et al., 2012). The main working mechanism of EEW is to rapidly determine the basic source parameters of the earthquake using near-field sites and release timely alarm information, so that emergency response agencies have enough time to take disaster mitigation actions. Although the emergency time provided by EEW is limited, it is of great significance for emergency response and disaster mitigation (Lee et al., 2011; Allen et al., 2019).

Most of the traditional methods conduct the inversion of source parameters using the seismic instrument. However, the seismic instrument often suffers from the problems such as saturation, tilt, and rotation, and thus cannot accurately monitor the ground displacement during the earthquake (Boore et al., 2005; Wu et al., 2007; Chao et al., 2010; Moya et al., 2016). As one of the representative technologies in the field of space geodesy, Global Navigation Satellite System (GNSS) has the advantages of high positioning accuracy, wide coverage, and all-weather continuous observation, which has become a powerful means to monitor the crustal deformation. With the development of GNSS positioning technology, the emergence of high-rate GNSS receivers has made it possible to detect short-period transient crustal deformation (Larson et al., 2003; Kouba et al., 2005; Avallone et al., 2011; Xu et al., 2013). High-rate GNSS (e.g., 1, 5, or 10 Hz) can detect the displacement with time scales of second or sub-second, which can capture the rapidly crustal motion during the earthquake. Compared with traditional GNSS or Interferometric Synthetic Aperture Radar (InSAR) observations, high-rate GNSS can accurately capture transient crustal movements (Bock et al., 2004; Irwan et al., 2004; Ohta et al., 2006; Smalley et al., 2009; Zhou et al., 2025). Meanwhile, high-rate GNSS can effectively overcome the problems encountered by traditional seismic instruments, and the ground displacement captured by high-rate GNSS is more accurate and reliable (Wang et al., 2003; Wang et al., 2007; Wang et al., 2011). Thus, high-rate GNSS is widely applied in the transient crustal deformation detection and source parameter inversion of the earthquake (e.g., Ebinuma et al., 2012; Crowell et al., 2018; Xiang et al., 2019; Melgar et al., 2020; Golriz et al., 2021; Golriz et al., 2023; Lin et al., 2023).

Cite this article as: Xiang Y, Hong L, Qin M, Bian Y: Rapid inversion of source parameters for the 2021 Chignik, Alaska earthquake using high-rate GNSS observations. Acta Geodyn. Geomater., 22, No. 4 (220), 473–484, 2025. DOI: 10.13168/AGG.2025.0034

On July 29, 2021 at 06:15:47 (UTC), an M 8.2 earthquake occurred off the coast of Alaska, USA. It is a typical megathrust earthquake that occurs in the subduction zone. Alaska is located at the junction of the Pacific Plate and the North American Plate, where the Pacific Plate subducts under the North American Plate. During the subduction process, the interaction between the Pacific Plate and the North American Plate leads to a large amount of stress accumulation. The megathrust earthquakes are caused by the accumulation and release of stress between the subducting plate and the overlying plate. The 2021 Chignik earthquake was the strongest earthquake in Alaska in recent years. The hypocenter was located along the Aleutian Islands, with a focal depth of about 32 km. The epicenter was located at the latitude of 55.325° N and the longitude of 157.841° W. The shaking was felt in most regions of Alaska. Whereas, as the hypocenter was deep and the destructive force was limited, no casualties or significant property losses were caused. There have been many strong earthquakes in this region, such as the 1964 Great Alaska Earthquake (Mw 9.2), which was the second largest earthquake recorded in history. GNSS sites are widely distributed in Alaska, with a focus on covering seismically and volcanically active regions. The coseismic crustal deformations caused by this earthquake are successfully recorded by near-field GNSS, providing important data sets for the rapid inversion of source parameters. Meanwhile, this earthquake also provides a good opportunity to explore the feasibility of using land GNSS sites for the EEW of strong earthquakes in offshore subduction zones.

In this paper, the coseismic dynamic and static deformations caused by the 2021 M 8.2 Chignik, Alaska earthquake are detected by the near-field high-rate GNSS sites. The noise reduction of high-rate GNSS displacement time series is performed to highlight the tectonic signal. Based on the high-rate GNSS displacement time series, the S-transform is adopted to detect the first arrival time of seismic waves at the GNSS sites in the time-frequency domain. Subsequently, the Peak Ground Displacement (PGD) is calculated using the GNSS displacement time series, and the moment magnitude of this earthquake is inverted according to the empirical regression model. Meanwhile, the convergence time of the moment magnitude inverted by GNSS sites is explored to discuss its feasibility for EEW. Finally, based on the GNSS-derived coseismic static deformations, the coseismic slip distribution of the earthquake is estimated under the layered Earth model to reveal the coseismic rupture properties.

2. 2DATA AND METHODS

2.1. TECTONIC SETTING AND GNSS DATA SETS

Alaska is located at the junction of the Pacific Plate and the North American Plate, which is a portion of the Aleutian subduction zone. In this region, the Pacific Plate moves northwestward at a speed of about 6-7 cm/yr and subducts under the North American Plate. It is also one of the regions with frequent seismic activities. In the Aleutian subduction zone, the subduction of the Pacific Plate causes a large amount of stress accumulation. When the stress exceeds the fracture strength of the rock, an earthquake will be generated to release the accumulated stress. The coseismic dynamic deformations caused by this earthquake are successfully recorded by the near-field GNSS site (Fig. 1). In order to detect the transient coseismic crustal deformations, the 1 Hz observations of the near-field GNSS site during the earthquake are collected, which is provided by the EarthScope Consortium. The GNSS data sets are solved using the Precise Point Positioning (PPP) software PPP-AR developed by the PRIDE research group of Wuhan University, China (Geng et al., 2019). Based on the PPP-AR software, the GNSS displacement time series of the above-mentioned near-field sites can be obtained. During data processing, the VMF1 mapping function is used to correct tropospheric delays, the GIM product is used to correct high-order ionospheric errors, and the effects of solid Earth tide, ocean tide, and polar tide are also corrected. Precise satellite orbit, satellite clock error, and phase deviation products adopt the products provided by Wuhan University, China.

2.2. SMOOTHING PRIORS METHOD

The Smoothness Priors Method (SPM) was proposed by Tarvainen et al. (2002), which can effectively separate nonlinear trend from non-stationary time series. GNSS displacement time series can be considered to be composed of nonlinear trend and seismic wave signal. The nonlinear trend component can be expressed as follows:

$$Z_{trend} = H\theta + \xi \tag{1}$$

Among them, $H \in R^{n\times m}$ represents the observation matrix, $\theta \in R^{m}$is the regression coefficient, and ξ is the observation error. Then, the regularized Least Squares Method (LSE) can be used to estimate the regression coefficient (i.e., $\hat{\theta}$):

$$\hat{\theta}_{\gamma}=\text{argmin}\{\|H\theta - z\|^2 + \gamma^2\|D_d(H\theta)\|^2\} \tag{2}$$

Where γ is the regularization coefficient, $D_d$is the discrete approximation of the derivative operation. The solution of the above formula can be expressed as follows:

$$\hat{\theta}_{\gamma} = (H^T\text{H}+\gamma^2 H^T D_d^T D_d)^{-1}H^T z \tag{3}$$

$$\hat{z}_{trend} = H\hat{\theta}_{\gamma} \tag{4}$$

Where $\hat{z}_{trend}$is the estimated nonlinear trend. The selection of observation matrix is based on the prior information of displacement time series.

2.3. S-TRANSFORMATION

S-transformation is a lossless and reversible non-stationary signal analysis method (Stockwell et al.,

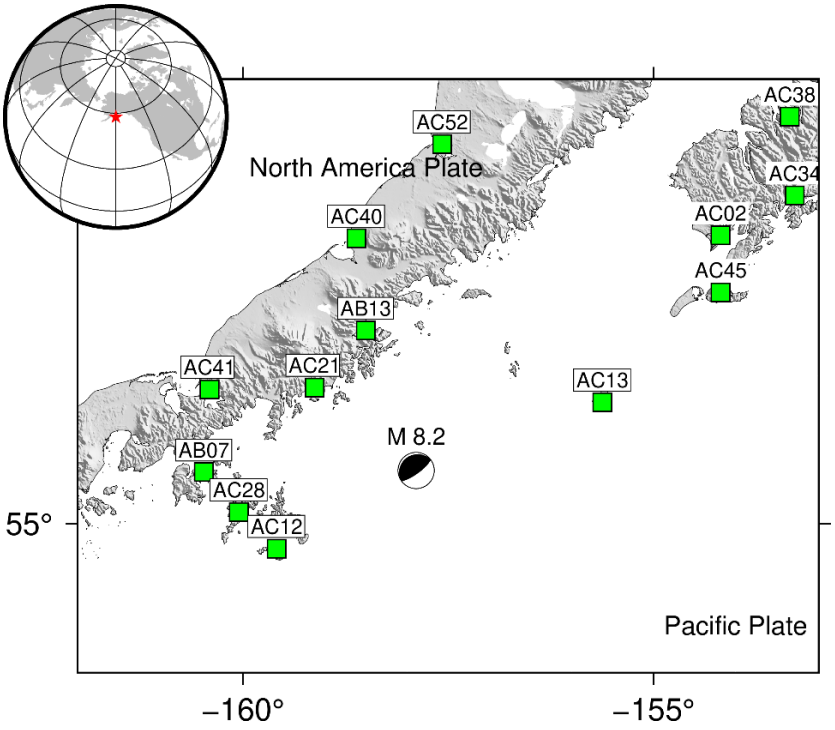

Fig. 1 Tectonic setting and spatial distribution of GNSS sites.

1996). This method combines the properties of Short-Time Fourier Transform (STFT) and Continuous Wavelet Transform (CWT), which can be regarded as a phase correction of CWT. If $h(t)$ represents the seismic wave signal, the S transform of the seismic wave signal is defined as:

$$S(\tau, f) = \int_{-\infty}^{\infty} h(t) \frac{|f|}{\sqrt{2\pi}} \mathrm{e}^{\frac{-(\tau-t)^2 f^2}{2}} \mathrm{e}^{-i2\pi ft} \mathrm{d}t \tag{5}$$

Among them, τ represents the smoothing factor of the Gaussian window function, f represents the frequency, and t represents the time.

The Gaussian window function and the basis wavelet are defined as:

$$g_f(t) = \frac{|f|}{\sqrt{2\pi}} e^{\left(-\frac{t^2 f^2}{2}\right)} \tag{6}$$

$$\omega_f(t) = \frac{|f|}{\sqrt{2\pi}} e^{\left(-\frac{t^2 f^2}{2} - i2f\pi t\right)} = g_f(t) = e^{\left(-\frac{t^2 f^2}{2} i2f\pi t\right)} \tag{7}$$

Therefore, the time window width of the S-transform is inversely proportional to the frequency, and sufficient time-frequency resolution can be obtained.

2.4. COSEISMIC FAULT SLIP INVERSION

Okada elastic dislocation theory is a spatial response of ground displacement to fault dislocation under a uniform half-space dislocation model. Wang et al. (2013) extended this theory to a layered half-space dislocation model and proposed the Steepest Descent Method (SDM). The fault slip distribution inversion is performed under the layered half-space Earth model. The inversion problem can be expressed as follows:

$$f(s) = \|y - Ms\|^2 + \beta^2 \|Hs\| \tag{8}$$

$$\|Hs\| = \left\| \frac{\partial^2}{\partial x^2} \tau(s) + \frac{\partial^2}{\partial y^2} \tau(s) \right\|^2 \tag{9}$$

Among them, y is the ground displacement, s is the fault dislocation, M is the Green's function calculated under the layered half-space Earth model, $\tau(s)$ is the stress drop, and β is the smoothing factor. $\|y - Ms\|^2$ represents the data misfit, and $\beta^2 \|Hs\|$ represents the model roughness. When inverting the fault slip distribution, the optimal solution can be obtained by minimizing both the data misfit and model roughness. The trade-off value between the data misfit and model roughness is usually chosen as the optimal smoothing factor.

3. RESULTS AND DISCUSSION

3.1. DETECTION OF COSEISMIC DEFORMATION

GNSS dynamic displacement time series can provide insight into seismic wave signals and reflect the dynamic crustal movements during the earthquake. Figure 2 displays the dynamic displacement time series of seven near-field GNSS sites. The amplitude of the dynamic displacement time series of GNSS sites gradually decreases as the epicentral distance increases. The focal mechanism solution indicates that this earthquake is caused by the rupture of a thrust fault in the NE-SW direction, and the site AC13 is located near the rupture direction of the seismogenic fault. Generally, the ground movement in the direction of the fault rupture is stronger, resulting in the largest displacement amplitude of site AC13, which is 52.42,

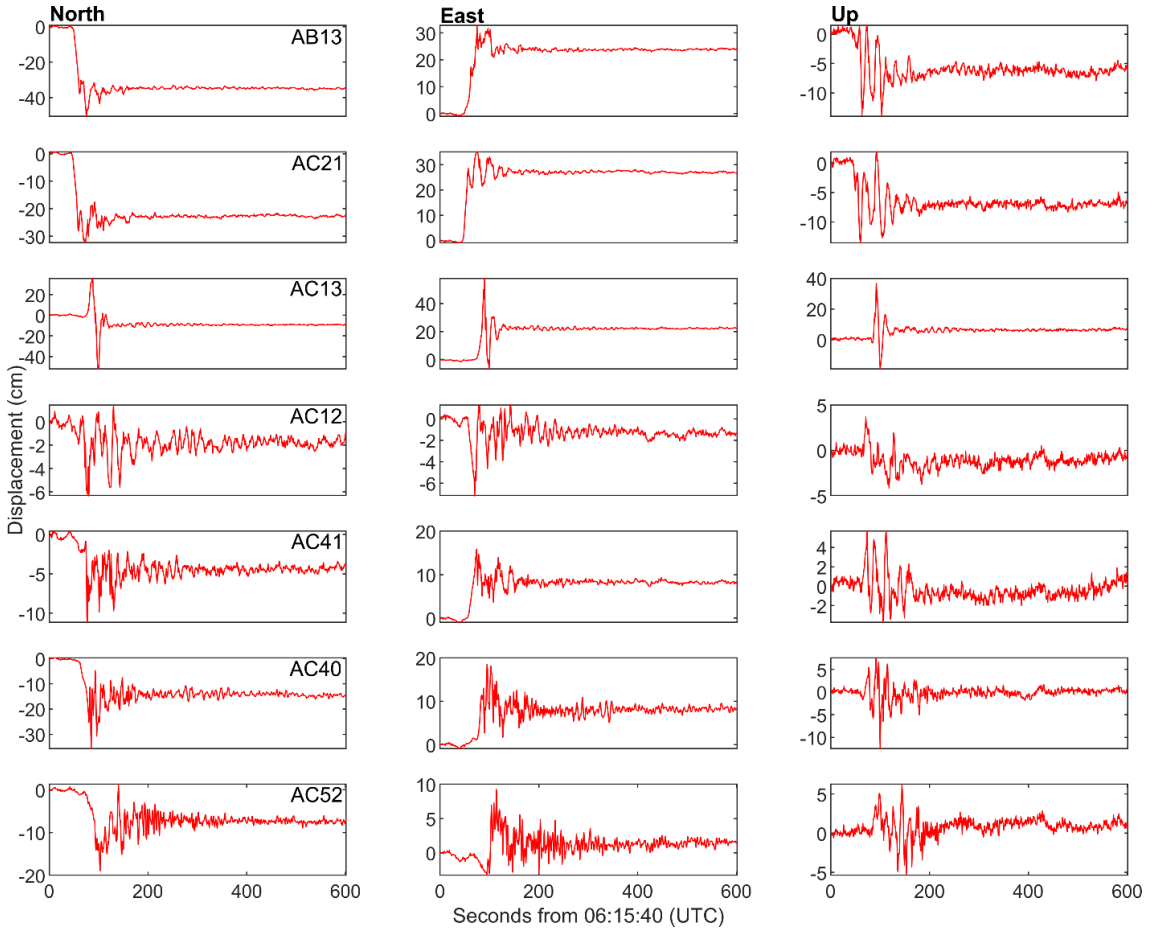

Fig. 2 Dynamic displacement time series of seven GNSS sites in the three components.

57.87, and 36.71 cm in the north, east, and up components, respectively. The next largest displacement amplitude values are generated at sites AB13 and AC21, which are 50.66, 32.86 and 14.02 cm and 32.44, 35.13 and 36.71 cm in the north, east, and up components, respectively.

Meanwhile, the horizontal motion trajectories of some representative GNSS sites in the near field are also revealed in this paper. Figure 3 depicts the horizontal motion trajectories of three near-field GNSS sites during the earthquake. In order to better show the horizontal motion properties of the GNSS site, we only display the horizontal motion trajectories of each site in the specific time periods. The selected time periods for sites AC13, AB13, and AC21 are 50~150 s, 40~120 s, and 40~120 s, respectively. The displacement amplitudes of site AC13 during the earthquake are the largest in the three components. In the horizontal direction, the site AC13 rotates clockwise and gradually moves to the southeast after the seismic wave arrival. Finally, the site AC stops in the southeast region of the starting position. Sites AB13 and AC21 are both located in the northwest region of the hypocenter. The site AB13 moves towards the southeast during the earthquake, and finally stops in the southeast region of the starting position after a period of irregular movement. The movement range of AB13 site in the east direction is 0~33 cm, and the movement range in the north direction is -55~0 cm. Since sites AB13 and AC21 are located close to each other, the two sites exhibit similar movement characteristics in the horizontal direction. The site AC21 also moves towards southeast during the earthquake and finally stops in the southeast region of the starting position. The movement range of site AC21 in the east direction is between 0 and 35 cm, and the movement range in the north direction is between -33 and 0 cm.

The static offset caused by an earthquake is the basic information required for EEW, which can be used to estimate the coseismic rupture process. Generally, the coseismic static offset can be determined by the difference of the daily GNSS solutions. The coseismic deformation determined by this method will include some very early postseismic deformation. Considering this problem, the SPM method is adopted to quickly extract the coseismic static offset from the high-rate GNSS displacement waveform in this paper. An important issue in extracting static offset using SPM is the selection of regularization parameters, and the cutoff frequency decreases as the regularization parameter increases. In general, the frequency range of seismic waves is 0.02~100 Hz, and the signal with a frequency greater

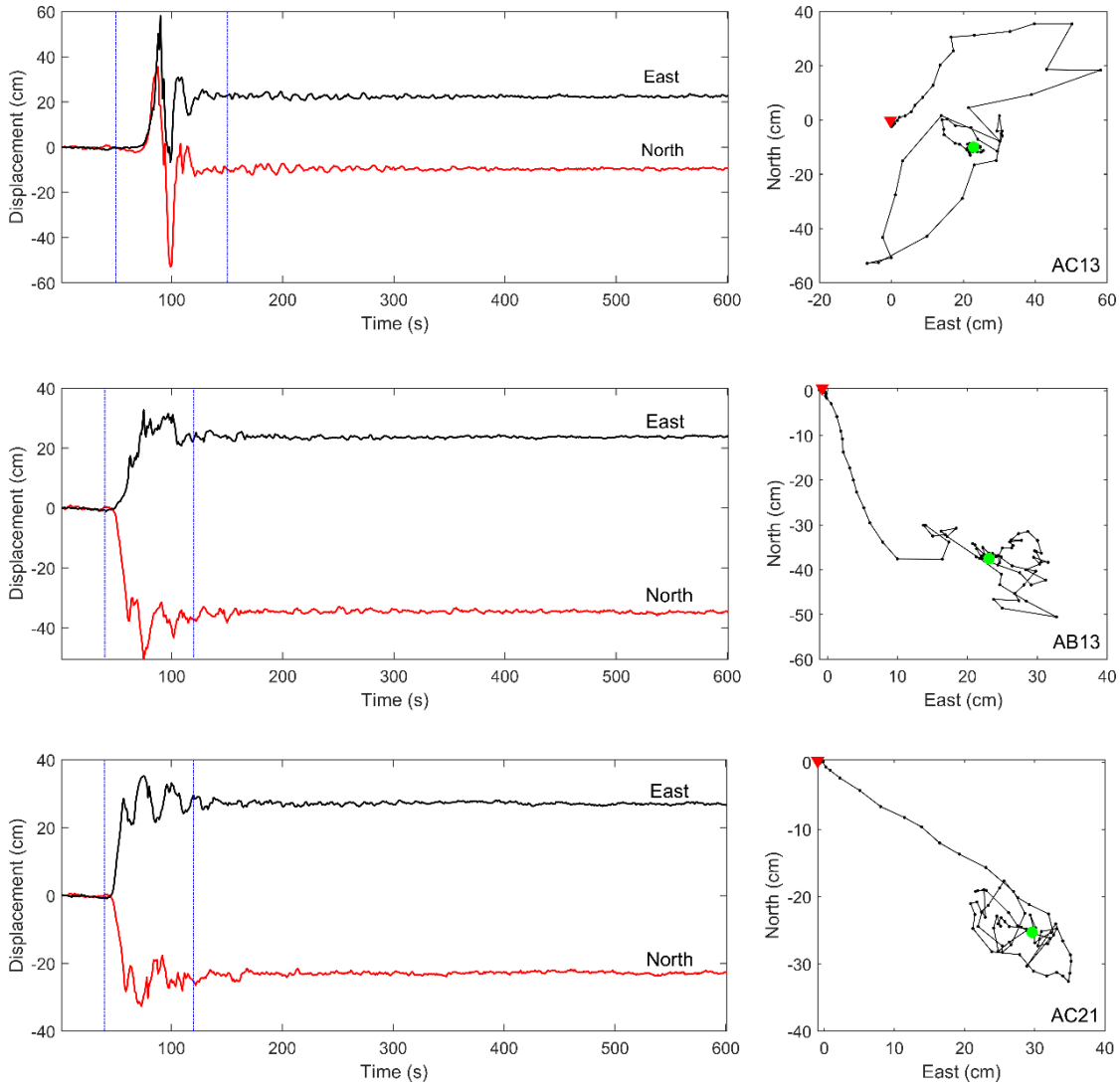

Fig. 3 Horizontal motion trajectories of three near-field GNSS sites during the earthquake.

than 0.02 Hz can be regarded as seismic wave signal. Thus, 0.02 Hz can be selected as the cutoff frequency, and its corresponding regularization parameter is 60.

Figure 4 describes the nonlinear trend and seismic wave signal extracted from the east component of the GNSS displacement waveform at site AC13. Based on the nonlinear trend signal, the estimated static offset of the east component of site AC13 is 239.33 mm, which is consistent with the result provided by EarthScope Consortium. Similarly, the SPM method is utilized to extract the static offset of the north component of site AC13. Due to the poor accuracy of the vertical component, we do not extract the static offset of the vertical component based on SPM. Table 1 lists the estimated static offset of the horizontal components of six sites, and the results provided by EarthScope Consortium are regarded as a reference. Through comparison, it can be seen that the SPM-estimated coseismic static offsets are slightly different from the reference values, indicating that high-rate GNSS can rapidly obtain reliable coseismic static offsets.

3.2. SEISMIC WAVE FIRST ARRIVAL DETECTION

Seismic wave first arrival detection is an important part of EEW, which is of great significance for postseismic emergency response. The seismic wave first arrival detection is conducted in the time-frequency domain based on S-transform. Due to the poor accuracy of the vertical component, the horizontal components of the GNSS displacement time series of nine sites are utilized to detect the first arrival of seismic wave. In order to reduce the influence of high-frequency noise and accurately detect the first arrival time of seismic wave, the wavelet denoising of GNSS displacement time series is firstly performed. Meanwhile, the velocity time series is extracted using the first-order difference, which can also weaken the influence of low-frequency nonlinear trend to a certain extent (Fig. 5). Secondly, the S-transform is adopted to process the preseismic velocity time series, taking it as the energy threshold of the background noise. On the basis of the energy threshold, the arrival time of seismic wave is detected by the energy spectrum of S-transform. Figure 6 shows

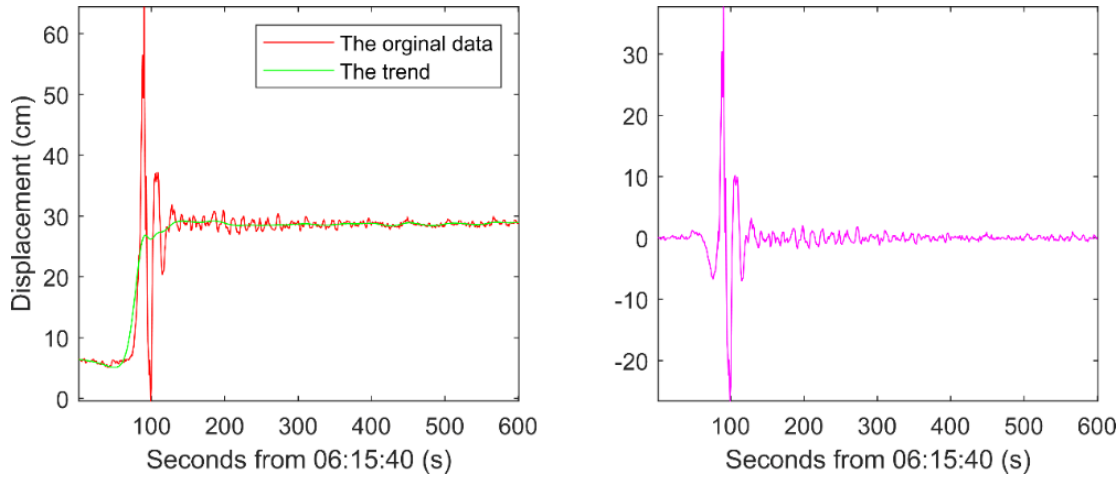

Fig. 4 SPM-smoothed result of the GNSS displacement waveform of site AC13 in the east component. (a) is the original waveform and the extracted nonlinear trend, and (b) is the extracted seismic wave signal.

Table 1 Static offsets of three GNSS sites in the east component.

Site	Epicentral distance (km)	SPM		EarthScope Consortium	
		E (mm)	N (mm)	E (mm)	N (mm)
AB07	163.638	49.10	-12.71	49.26	-14.78
AB13	111.715	254.82	-366.63	255.91	-369.20
AC13	151.204	239.33	-141.96	243.98	-146.94
AC21	99.451	287.68	-241.71	291.13	-243.12
AC40	179.956	82.66	-145.40	86.30	-152.32
AC41	169.310	85.69	-42.01	89.86	-47.50

the result of the seismic wave arrival detection using the horizontal components of the velocity time series of site AC13. The red arrow indicates the first arrival time of seismic wave detected by the S-transform spectrum of velocity time series. The S-transform spectrum occurs obvious energy changes after the seismic wave propagates to the GNSS site. The moment when the energy changes is the first arrival time of seismic wave. According to the S-transform spectrum, the estimated first arrival times of the seismic waves detected by the north and east components of site AC13 are 06:16:32 and 06:16:42 (UTC), respectively. The average propagation time of seismic wave detected by site AC13 is about 37 s.

Similarly, the other six sites are also utilized to detect the first arrival time of seismic wave. According to the epicentral distance and the propagation time of seismic wave, the propagation velocity of seismic wave is calculated (Table 2). In general, the theoretical value of P-wave propagation velocity ranges from 5 to 8 km/s. Thus, the GNSS-estimated propagation velocities are not within the range, indicating that the disturbance of GNSS site may be caused by S-wave or seismic surface waves. It is worth noting that the energy of seismic waves will decay with the increase of epicentral distance. In theory, the first arrival should be the P-wave because the P-wave has the fastest propagation speed. However, considering the energy attenuation of seismic wave during propagation, the weak P wave signal may not be detected, and the disturbance of GNSS site may be S-wave or surface waves. For this earthquake, the hypocenter is located in the offshore region of Alaska, and the weak P-wave signal is difficult to be detected by land-based GNSS sites. Therefore, for this earthquake, the first arrival seismic wave detected by the GNSS sites located in the Alaska Peninsula may be P-wave, S-wave or surface waves.

3.3. MOMENT MAGNITUDE INVERSION

Considering that the GNSS displacement waveform with a low signal-to-noise ratio is difficult to accurately detect P-wave, it may not be reasonable to utilize the PGD within a few seconds after P-wave arrival to determine the magnitude. Meanwhile, the GNSS site directly measures the ground displacement, meaning that the GNSS site can accurately detect the PGD. Thus, the PGD obtained by GNSS site is adopted to invert the moment magnitude of the earthquake according to the empirical regression model in this paper. In order to determine the moment magnitude of the earthquake, we adopt the empirical formula proposed by Crowell et al. (2013):

$$log(PGD) = A + B * M_w + C * M_w * log(R) \quad (10)$$

Where *Mw* is the moment magnitude and *R* is the epicentral distance. *A*, *B*, and *C* are regression coefficients determined by Melgar et al. (2015) (i.e., A = -4.434 ± 0.141, B = 1.047 ± 0.022, C = - 0.138 ± 0.003). The calculation formula of PGD can be defined as:

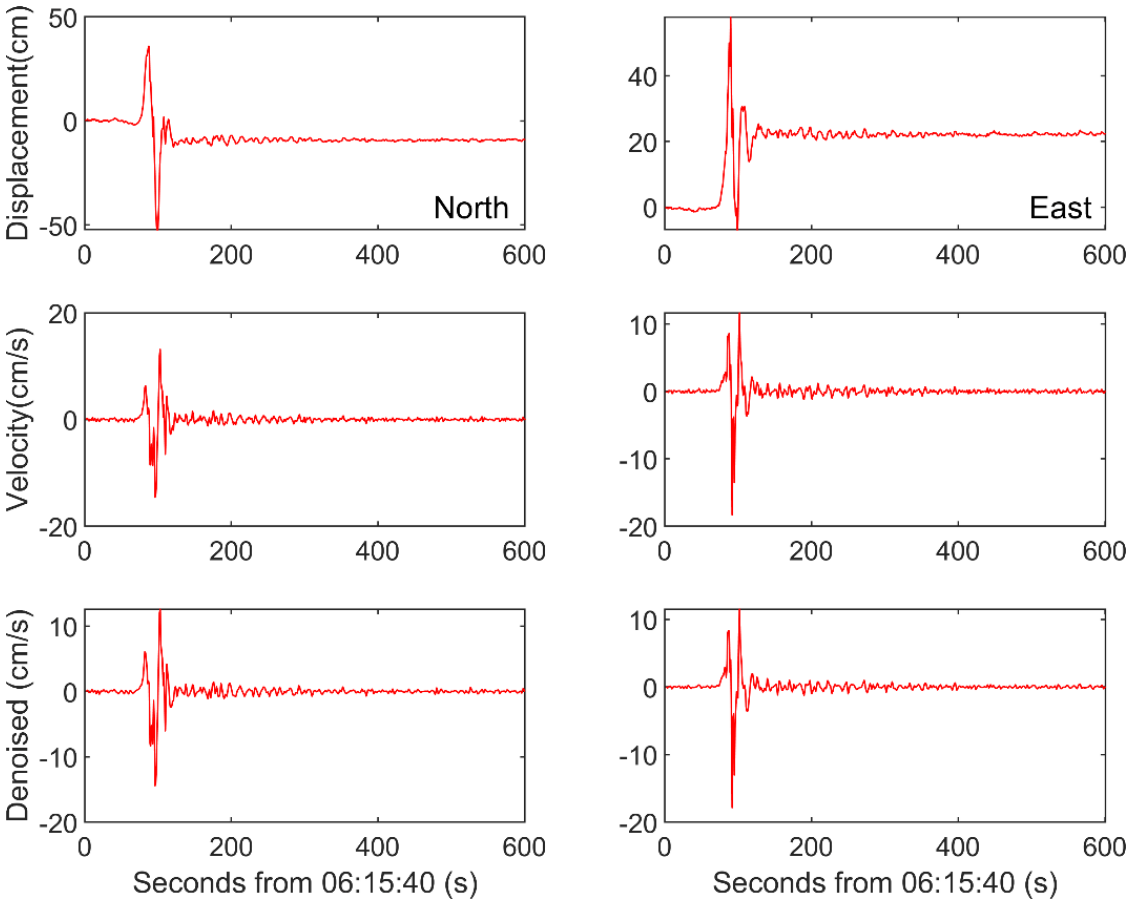

Fig. 5 The displacement, velocity, and denoised velocity time series of GNSS site AC13 in the north and east components.

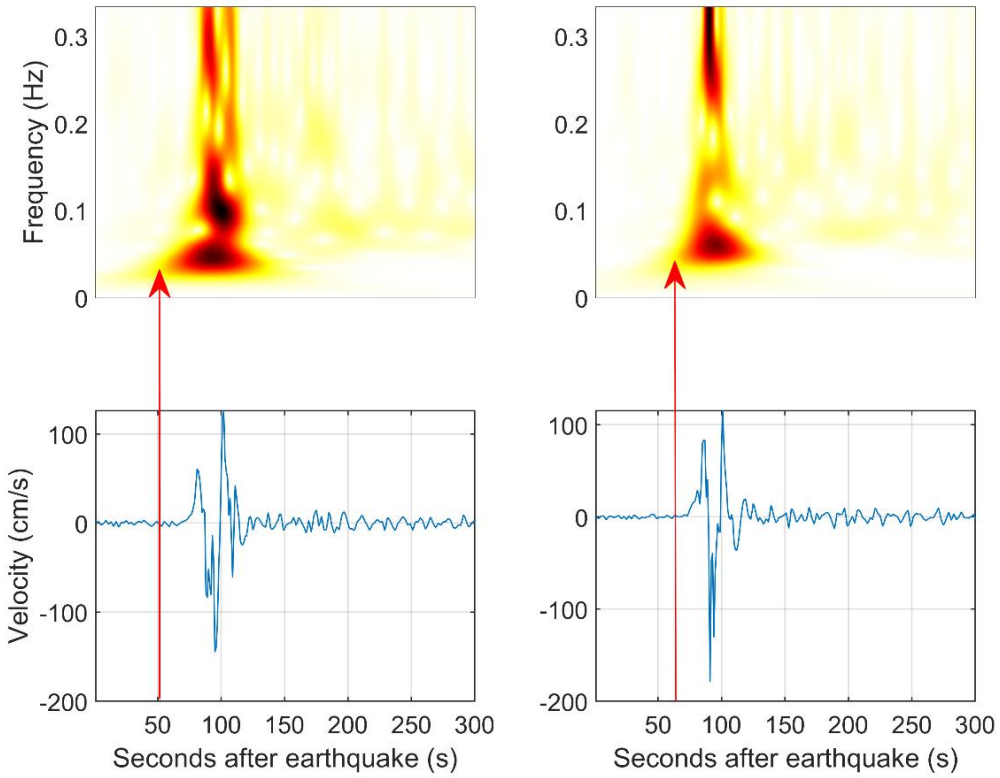

Fig. 6 Velocity time series and the corresponding S-transform spectrum of GNSS site AC13 in the horizontal components.

Table 2 Detection results of seismic wave arrival time.

Site	Epicentral distance	Arrival time of seismic wave (UTC)		Average propagation time (s)	Speed (km/s)
		North	East		
AB07	163.638	06:16:40	06:16:36	51	3.209
AB13	111.715	06:16:20	06:16:30	38	2.939
AC12	123.418	06:16:31	06:16:33	45	2.743
AC13	151.204	06:16:30	06:16:40	48	3.150
AC21	99.451	06:16:00	06:16:10	18	5.525
AC40	179.956	06:16:40	06:16:40	53	3.395
AC41	169.311	06:16:40	06:16:36	51	3.320

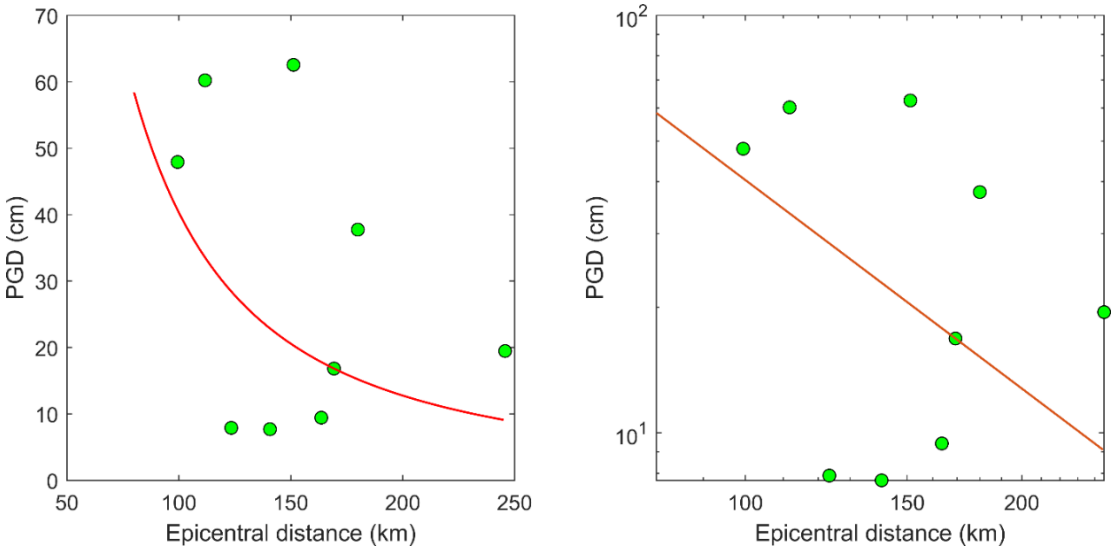

Fig. 7 Relationship between PGD of horizontal components with epicenter distance for nine GNSS sites.

$$PGD = max(\sqrt{[N(t)^2 + E(t)^2 + U(t)^2]}) \quad (11)$$

Where N(t), E(t) and U(t) are the displacement time series in the north, east, and up components. Previous studies suggest that PGD values approximately decay with $r^{-1.66}$, and this decay relationship can be used to estimate the magnitude (Crowell et al., 2009). According to formula (11), the PGD value of each site is calculated using the GNSS displacement waveform. As depicted in Figure 7, the PGD values are distributed around the solid line, indicating that PGD values decay with $r^{-1.66}$. Thus, this relationship can be used to estimate the moment magnitude of this earthquake.

Based on PGD values, the above empirical regression model is utilized to invert the moment magnitude of this earthquake. As described in Figure 8, the estimated moment magnitudes of nine sites range from Mw 7.03 to 8.35, with an average of Mw 7.74. The average moment magnitude deviates from the USGS-released reference magnitude (Mw 8.2) by 0.46. The result indicates that the empirical regression model is suitable for the moment magnitude inversion of this earthquake. Overall, the moment magnitudes inverted by GNSS sites are relatively small, mainly due to the fact that the hypocenter of the earthquake is located in the offshore region, and the influence of seismic waves on land-based GNSS sites is weakened to a certain extent. In terms of spatial distribution, the larger magnitude inverted by site AC13 is mainly attributed to the fact that the site is located in the direction of the fault rupture, which generates larger ground displacement during the earthquake. The moment magnitudes determined by the three stations located southwest of the hypocenter are relatively small, especially at site AC12. In contrast, the magnitudes inverted by several sites located on the north side are closest to the reference magnitude.

Also, the time evolution of the moment magnitude estimated by each GNSS site and the average moment magnitude determined by the nine sites is also explored. Taking the moment of earthquake occurrence as the initial time, the PGD value of each GNSS station is continuously updated until the estimated moment magnitude converges. As shown in Figure 10, the convergence time of the moment magnitudes determined by the nine sites ranges from 64 to 117 s. The convergence time of average moment magnitude (i.e., Mw 7.74) is 117 s, indicating that the nine sites can obtain a robust and reliable magnitude about 117 s after the earthquake. In

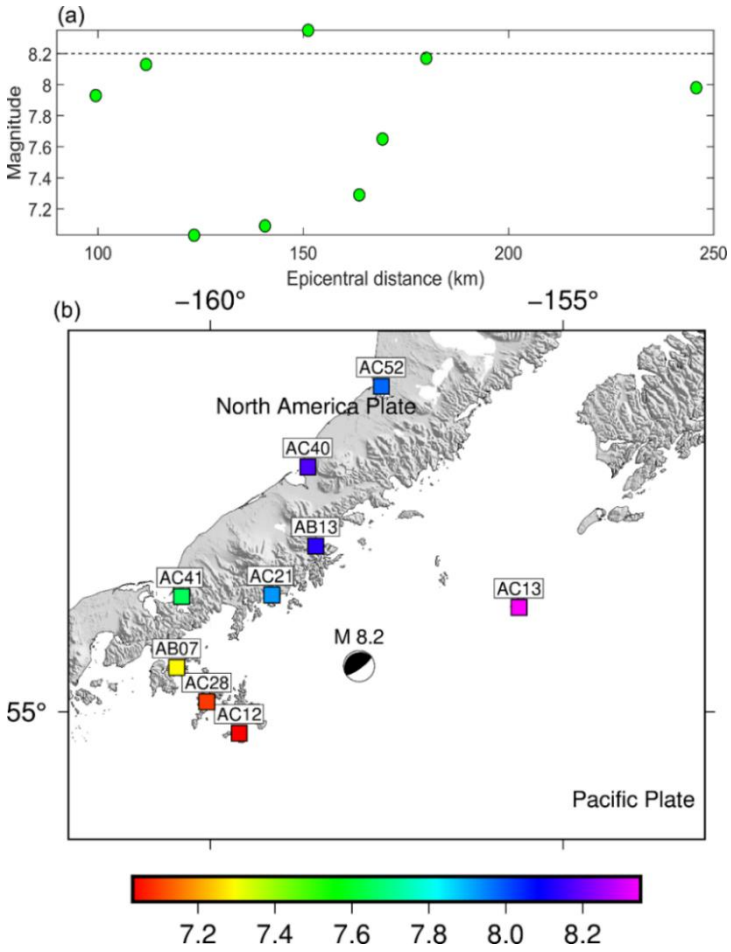

Fig. 8 Comparison of moment magnitudes estimated by nine GNSS sites with reference magnitudes.

the EEW, it is necessary to select some near-field GNSS sites to determine the warning magnitude, which can realize the rapid warning of the earthquake. Crowell et al. (2013) suggested that the number of GNSS sites used for EEW should not be less than four. In order to realize the rapid warning of this earthquake, we conduct the joint warning based on four GNSS sites in this paper. Meanwhile, the effect of spatial distribution of GNSS stations on magnitude estimation is investigated. Based on the convergence time of the estimated magnitude, four GNSS sites (AB07, AC12, AC13, and AC21) are firstly selected from all the sites for the early warning magnitude estimation. Meanwhile, considering the influence of the spatial distribution of GNSS sites, the site AC41 site is replaced by site AC02. Figure 11 describes the time evolution of the average magnitude measured by nine GNSS sites, four GNSS site combination-1 (i.e., AB07, AC12, AC28, and AC41) and four GNSS site combination-2 (i.e., AB07, AC12, AC28, and AC02). The moment magnitude estimated by the four GNSS site combination-2 is more reliable and accurate, and the convergence time for obtaining a robust moment magnitude is shorter. Based on the above results, it can be seen that the rapid determination of the moment magnitude based on the high-rate GNSS can realize the early warning of this earthquake. In addition, the estimated magnitude will be affected by the spatial distribution of GNSS sites. Selecting suitable sites according to the spatial distribution of each site can obtain a more reliable and accurate warning magnitude, which can realize the EEW of this earthquake.

3.4. INVERSION OF COSEISMIC RUPTURE DISTRIBUTION

Following the earthquake, USGS adopted 44 teleseismic P waves, 16 SH waves, and 60 long-period surface waves to construct a coseismic rupture model. The focal mechanism solution indicates that the strike and dip of the earthquake are 243° and 14°, respectively. Based on the information released by USGS, a fault model with the length and width of 297.5 and 200 km along the strike and dip directions is constructed. The fault model is divided into the sub-fault with the size of 10×10 km, and the number of sub-faults is 600. Meanwhile, the EDGRN code developed by Wang et al. (2003) is utilized to calculate the dislocation Green's function, and the USGS-provided Earth model parameters is adopted. In order to obtain a smooth and accurate slip model, the optimal smoothing factor is determined according to the weight of data misfit and model roughness. The trade-off value of data misfit and model roughness is taken as the optimal smoothing factor.

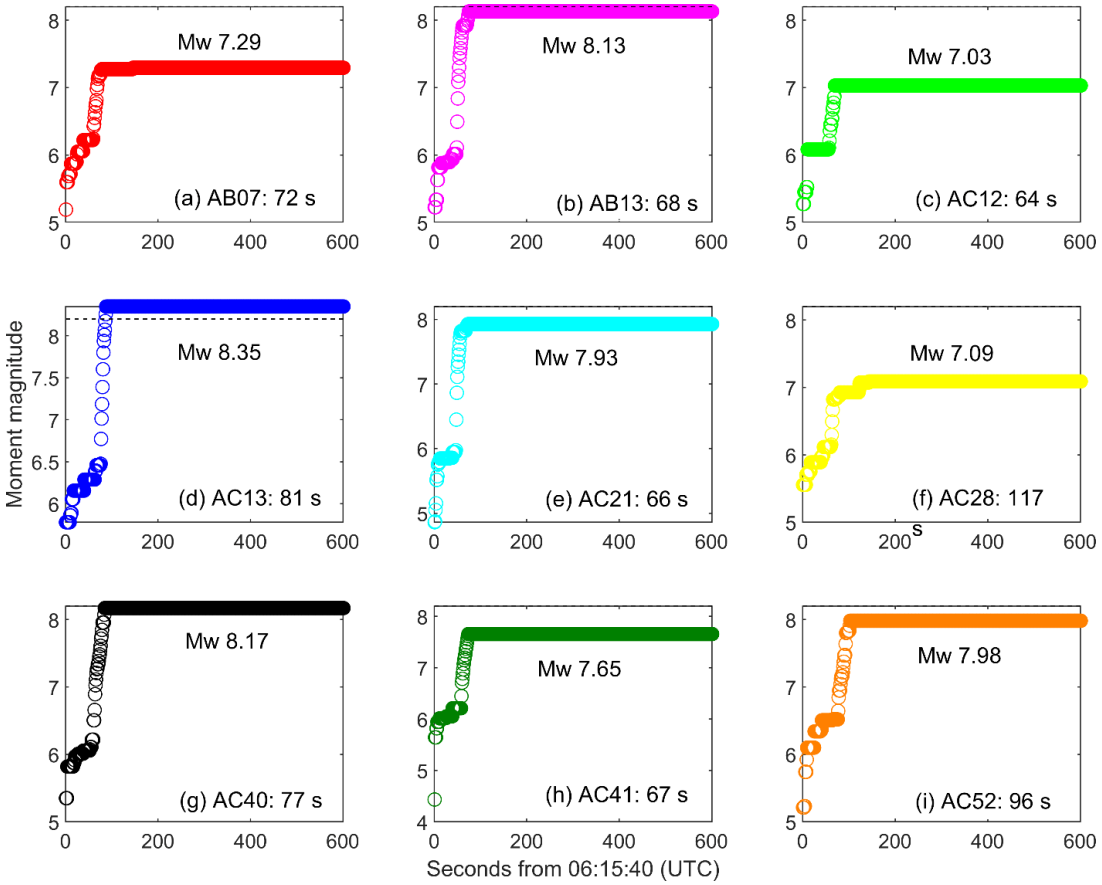

Fig. 9 Convergence process of the estimated moment magnitude s of nine GNSS sites.

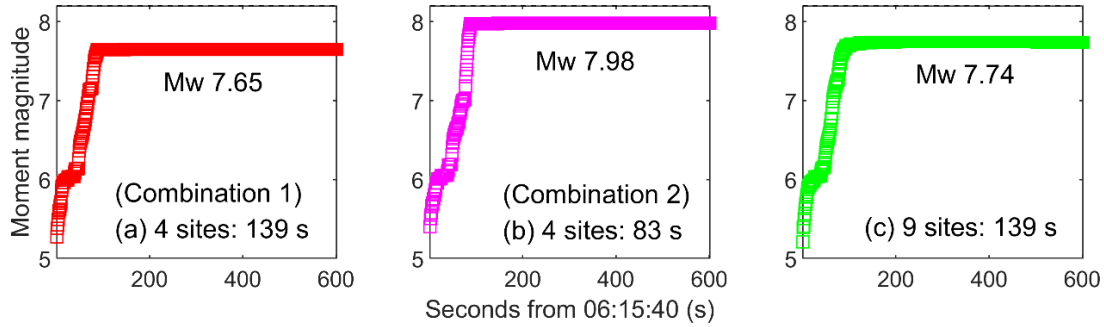

Fig. 10 Time evolution of moment magnitude inverted by different site combinations.

Based on the GNSS-derived coseismic static deformations and the fault model, the SDM program is performed to invert the coseismic rupture distribution of this earthquake under the layered Earth model. The 2D and 3D patterns of coseismic rupture are exhibited in Figure 11. This earthquake is a typical single-fault rupture mode, and the coseismic fault slip is distributed on a seismogenic fault with the dip of 14°. The coseismic rupture distribution is mainly concentrated between 20 and 50 km in depth. The maximum value of coseismic slip is 3.87 m, located at longitude 157.6°W, latitude 55.5°N, and depth 33.9 km. The seismic moment released by this earthquake is equivalent to an earthquake with a moment magnitude of Mw 8.0. The correlation coefficient between the GNSS-observed and SDM-simulated coseismic offsets reaches 0.97. Previous studies have investigated the coseismic rupture pattern and the rupture process of this earthquake based on various geodetic observations (e.g., GNSS, InSAR, and seafloor geodetic observations) and seismic data sets. For the coseismic rupture pattern of this earthquake, our inversion result is in good agreement with the previous studies, which confirms the reliability of the coseismic rupture inversion in this paper. In addition, the magnitude of the coseismic rupture distribution is slightly smaller because the high-rate GNSS is utilized to estimate the coseismic static deformations, and the very early postseismic deformations is eliminated to a certain extent.

4. CONCLUSION

In this paper, the high-rate GNSS is utilized to detect the transient coseismic crustal deformation

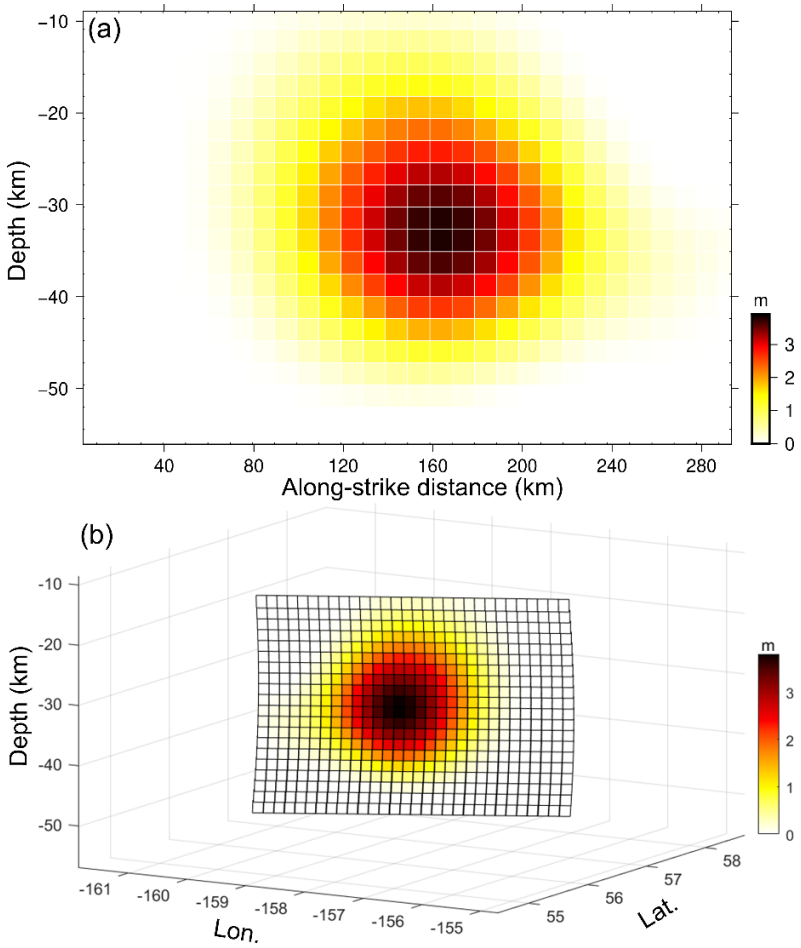

Fig. 11 2D (a) and 3D (b) spatial distribution of coseismic rupture of the 2021 M 8.2 Chignik earthquake.

caused by the 2021 M 8.2 Chignik, Alaska earthquake. The properties of crustal movement during the earthquake are investigated based on GNSS dynamic displacement, and the SPM-based extracted nonlinear trend is adopted to estimate the coseismic offsets. Considering that the high-rate GNSS displacement waveform has a low signal-to-noise ratio, the GNSS displacement time series is denoised by the wavelet denoising method to further highlight the seismic wave signal. Based on the PGD captured by GNSS site, and the moment magnitude of the earthquake is rapidly inverted according to the magnitude regression model. The result indicates that high-rate GNSS can rapidly invert the moment magnitude of the earthquake, and the average magnitude is only 0.46 magnitude different from the reference magnitude released by USGS. Finally, based on the SPM-based extracted GNSS coseismic static deformation, the coseismic slip distribution of the earthquake is inverted under the layered Earth model. The correlation coefficient between the GNSS-observed and SDM-simulated coseismic deformations is 0.97. The result of coseismic slip inversion is consistent with that released by USGS, which verifies the reliability of the coseismic rupture inversion in this paper.

ACKNOWLEDGEMENT

We are very grateful to the EarthScope Consortium and the PRIDE Laboratory of Wuhan University for providing high-rate GPS data sets and the PPP-AR software. This study is support by the National Natural Science Foundation of China (No. 42304016, Funder: Yunfei Xiang).

REFERENCES

Allen, R.M. and Melgar, D.: 2019, Earthquake early warning: Advances, scientific challenges, and societal needs. Annu. Rev. Earth Planet. Sci., 47, 361–388. DOI: 10.1146/annurev-earth-053018-060457

Avallone, A., Marzario, M., Cirella, A. and Piatanesi, A.: 2011, Very high rate (10 Hz) GPS seismology for moderate-magnitude earthquakes: The case of the Mw 6.3 L'Aquila (central Italy) event. J. Geophys. Res., Solid Earth, 116, B02305. DOI: 10.1029/2010JB007834

Boore, D.M. and Bommer, J.J.: 2005, Processing of strong-motion accelerograms: needs, options and consequences. Soil Dyn. Earthq. Eng., 25, 2, 93–115. DOI: 10.1016/j.soildyn.2004.10.007

Bock, Y., Prawirodirdjo, L. and Melbourne, T.I.: 2004, Detection of arbitrarily large dynamic ground motions with a dense high-rate GPS network. Geophys. Res. Lett., 310, 6, 177–182. DOI: 10.1029/2003GL019150

Chao, W.A., Wu, Y.M., Zhao, L.: 2010, An automatic scheme for baseline correction of strong-motion records in co-seismic deformation determination. J. Seismol., 14, 3, 495–504. DOI: 10.1007/s10950-009-9178-7

Crowell, B.W., Schmidt, D.A., Bodin, P. et al.: 2018, G-FAST earthquake early warning potential for great earthquakes in Chile. Seismol. Res. Lett., 89, 2A, 542–556. DOI: 10.1785/0220170180

Crowell, B.W., Bock, Y. and Squibb, M.B.: 2009, Demonstration of earthquake early warning using total displacement waveforms from real time GPS networks. Seismol. Res. Lett., 80, 5, 772–782. DOI: 10.1785/gssrl.80.5.772

Crowell, B.W., Melgar, D., Bock, Y. et al.: 2013, Earthquake magnitude scaling using seismogeodetic data. Geophys. Res. Lett., 40, 23, 6089–6094. DOI: 10.1002/2013GL058391

Ebinuma, T. and Kato, T.: 2012, Dynamic characteristic of very-high-rate GPS observations for seismology. Earth Planets Space, 64, 369–377. DOI: 10.5047/eps.2011.11.005

Geng, J., Chen, X., Pan, Y., Mao, S., Li, C., Zhou, J. and Zhang, K.: 2019, PRIDE PPP-AR: an open-source software for GPS PPP ambiguity resolution. GPS Solut., 23, 91, 1–10. DOI: 10.1007/s10291-019-0888-1

Golriz, D., Bock, Y. and Xu, X.: 2021. Defining the coseismic phase of the crustal deformation cycle with seismogeodesy. J. Geophys. Res., Solid Earth, 126, e2021JB022002. DOI: 10.1029/2021JB022002

Golriz, D., Hirshorn, B., Bock, Y., Weinstein, S. and Weiss, J.R.: 2023, Real-time seismogeodetic earthquake magnitude estimates for local tsunami warnings. J. Geophys. Res., Solid Earth, 128, e2022JB025555. DOI: 10.1029/2022JB025555

Kouba, J.: 2005, A possible detection of the 26 December 2004 great Sumatra-Andaman Island earthquake with solution products of the international GNSS service. Stud.eophys. Geod., 49, 463–483. DOI: 10.1007/s11200-005-0022-4

Larson, K.M., Bodin, P. and Gomberg, J.: 2003, Using 1-Hz GPS data to measure Kouba deformations caused by the Denali fault earthquake. Science, 300, 5624, 1421–1424. DOI: 10.1126/science.1084531

Lee, W.H.K. and Wu, Y.M.: 2011, Earthquake monitoring and early warning systems. In: Meyers, R. (ed.), Extreme Environmental Events. Springer, New York, 278–311. DOI: 10.1007/978-1-4419-7695-6_18

Lin, J.T., Melgar, D., Sahakian, V.J., Thomas, A.M. and Searcy, J.: 2023. Real-time fault tracking and ground motion prediction for large earthquakes with HR-GNSS and deep learning. J. Geophys. Res., Solid Earth, 128, e2023JB027255. DOI: 10.1029/2023JB027255

Man, W. and Gao, J.: 2009, Statistical denoising of signals in the S-transform domain. Comput. Geosci., 35, 1079–1086.

Melgar, D., Crowell, B.W., Geng, J. et al.: 2015, Earthquake magnitude calculation without saturation from the scaling of peak ground displacement. Geophys. Res. Lett., 42, 13, 5197–5205. DOI: 10.1002/2015GL064278

Melgar, D., Crowell, B.W., Melbourne, T.I., Szeliga, W., Santillan, M. and Scrivner, C.: 2020, Noise characteristics of operational real-time high-rate GNSS positions in a large aperture network. J. Geophys. Res., Solid Earth, 125, 7, e2019JB019197. DOI: 10.1002/essoar.10501291.1

Moya, L., Yamazaki, F. and Liu, W.: 2016, Comparison of coseismic displacement obtained from GEONET and seismic networks. J. Earthq. Tsunami, 10, 2, 1640002. DOI: 10.1142/S1793431116400029

Ohta, Y., Meilano, I., Sagiya, T., Kimata, F. and Hirahara, K.: 2006, Large surface wave of the 2004 Sumatra-Andaman earthquake captured by the very long baseline kinematic analysis of 1-Hz GPS data. Earth Planets Space, 58, 2, 153–157. DOI: 10.1186/BF03353372

Smalley, R.: 2009, High-rate GPS: how high do we need to go? Seismol. Res. Lett., 80, 6, 1054–1061. DOI: 10.1785/gssrl.80.6.1054

Stockwell, R.G., Mansinha, L. and Lowe, R.P.: 1996, Localization of the complex spectrum: the S transform. IEEE Trans. Signal Process., 44, 998–1001. DOI: 10.1109/78.492555

Tarvainen, M.P., Ranta-Aho, P.O. and Karjalainen, P.A.: 2002, An advanced detrending method with application to HRV analysis. IEEE Trans. Biomed. Eng., 49, 2, 172. DOI: 10.1109/10.979357

Wang, G.Q., Boore, D.M., Igel, H. and Zhou, X.Y.: 2003, Some observations on colocated and closely spaced strong ground-motion records of the 1999 Chi-Chi, Taiwan, earthquake. Bull. Seismol. Soc. Am., 93, 2, 674–693. DOI: 10.1785/0120020045

Wang, G.Q., Boore, D.M., Tang, G. and Zhou, X.: 2007, Comparisons of ground motions from colocated and closely spaced one-sample-per-second global positioning system and accelerograph recordings of the 2003 M 6.5 San Simeon, California, earthquake in the Parkfield region. Bull. Seismol. Soc. Am., 97, 1 B, 76–90. DOI: 10.1785/0120060053

Wang, R., Martin, F.L. and Roth, F.: 2003, Computation of deformation induced by earthquakes in a multi-layered elastic crust—FORTRAN programs EDGRN/EDCMP. Comput. Geosci., 29, 2, 195–207. DOI: 10.1016/S0098-3004(02)00111-5

Wang, R., Diao, F. and Hoechner, A.: 2013, SDM–a geodetic inversion code incorporating with layered crust structure and curved fault geometry. Proceedings of the EGU General Assembly, 15, EGU2013–2411-1.

Wang, R.J., Schurr, B., Milkereit, C. et al.: 2011, An improved automatic scheme for empirical baseline correction of digital strong motion records. Bull. Seismol. Soc. Am., 101, 5, 2029–2044. DOI: 10.1785/0120110039

Wu, Y.M: 2007, Approximate recovery of coseismic deformation from Taiwan strong-motion records. J. Seismol., 11, 2, 159–170. DOI: 10.1007/s10950-006-9043-x

Xiang, Y.F., Yue, J.P., Tang, K. and Li, Z.: 2019, A comprehensive study of the 2016 Mw 6.0 Italy earthquake based on high-rate (10 Hz) GPS data. Adv. Space Res., 63, 1, 103–117. DOI: 10.1016/j.asr.2018.08.027

Zhang, X., Guo, F., Guo, B.F. et al.: 2012, Coseismic displacement monitoring and wave picking with high-rate GPS. Chinese J. Geophys., 55, 6, 1912–1918. DOI: 10.6038/j.issn.0001-5733.2012.06.012

Zhou, Y., He, X., Montillet, J.P., Wang, S., Hu, S., Sun, X., Huang, J. and Ma, X.: 2025. An improved ICEEMDAN-MPA-GRU model for GNSS height time series prediction with weighted quality evaluation index. GPS Solut., 29, 3, 1–19. DOI: 10.1007/s10291-025-01867-z